FRAMEWORK MATERIALS

Sequencing of metals in multivariate metal-organic frameworks

Zhe Ji[1,2,3,4], Tong Li[5]*, Omar M. Yaghi[1,2,3,4,6]*

We mapped the metal sequences within crystals of metal-oxide rods in multivariate metal-organic framework–74 containing mixed combinations of cobalt (Co), cadmium (Cd), lead (Pb), and manganese (Mn). Atom probe tomography of these crystals revealed the presence of heterogeneous spatial sequences of metal ions that we describe, depending on the metal and synthesis temperature used, as random (Co, Cd, 120°C), short duplicates (Co, Cd, 85°C), long duplicates (Co, Pb, 85°C), and insertions (Co, Mn, 85°C). Three crystals were examined for each sequence type, and the molar fraction of Co among all 12 samples was observed to vary from 0.4 to 0.9, without changing the sequence type. Compared with metal oxides, metal-organic frameworks have high tolerance for coexistence of different metal sizes in their rods and therefore assume various metal sequences.

Multivariate metal-organic frameworks (MOFs), in which either multiple organic functionalities (*1*) or metal ions (*2*) (variate units) are incorporated into their backbone, are capable of highly selective separations (*3*–*6*) and catalysis (*7*–*12*), exceeding in performance their less functionalized "simple" counterparts. Although the identity and ratio of the variate units can be readily quantified for these MOFs, determining their spatial arrangements remains a challenge. On the conceptual level, the sequences that the variate units may have in a MOF is likened to that of nucleotides in DNA (*13*). The arrangements of the variate units in MOFs introduce, as do the nucleotides in DNA, what we consider "heterogeneity within order" (*14*). The heterogeneity describes the changing spatial arrangements of the variate units, which are covalently bound to an otherwise ordered, translationally symmetric backbone.

We focused on mixed metals in infinite metal-oxide rods [known as secondary building units (SBUs)] (*15*) because such rods are well represented in MOFs (*16*), most especially those exhibiting unusual properties such as carbon capture (*17*–*19*) and water harvesting (*20*, *21*). Because these rods are atomically defined, they can be considered as thin fragments of metal oxides for which the arrangements of mixed metals have been examined (*22*–*25*). We sought to apply similar techniques to mixed-metal rod MOFs and recognized the potential for finding varying distributions of metals. In this study involving MOFs of this kind, the metals are known to be arranged along the rod in a "chain" configuration. Their spatial arrangement may follow many different scenarios, among which we consider four categories: random (uniform distribution), short and long duplicates (metals of the same kind adjacent to each other, and their number is defined as duplicate size), and insertions (a metal inserted in the duplicates of another metal type) (Fig. 1). The duplicates and insertions show recognizable regularity relative to that of the random category. We viewed each one of these as a metal sequence running along the rod, and therefore it was reasonable to expect that such sequences may form the basis for tunable gas adsorption and separation, effective polarization of incoming guest molecules, and highly selective catalysis along a cascade of heterometals.

The heterogeneity in DNA is characterized by means of sequencing using enzymes, but for MOFs, the conventional characterization methods, such as x-ray crystallography and nuclear magnetic resonance, are not as helpful because they measure statistical averages over bulk samples. Previously, attempts have been made to decipher heterogeneity of variate units in multivariate MOFs by using these techniques (*7*, *26*, *27*); however, molecular-level sequencing and obtaining real-space information remain an outstanding challenge. Because heterogeneity in variate units in MOFs manifests itself on the molecular level, it further complicates analysis by use of electron (*28*) and fluorescent microscopy imaging techniques (*29*). Fundamentally, there has been no method to distinguish MOF crystals of the same compound that are synthesized with the same composition of metals, in which the metals may very well adopt different sequence types. In general, the lack of capability to characterize mixed-metal MOFs has impeded their study and the development of more complex systems. In this contribution, we show how atom probe tomography (APT) (Fig. 1) can provide useful information in characterizing mixed-metal rod MOFs.

We chose the well-known structure of MOF-74 (*15*) to perform our APT studies. This structure is composed of metal-oxide rod SBUs joined by organic linkers to form a honeycomb pattern of rods and pores propagating along the crystallographic *c* axis (Fig. 1, along the *z* direction). It crystallizes into hexagonal-prism–shaped single crystals, and the metal-oxide rods run parallel to the long dimension of these crystals (Fig. 2A). A binary combination of cobalt (Co), cadmium (Cd), lead (Pb), and manganese (Mn) ions were used to synthesize the mixed-metal MOF-74 crystals. These metals were chosen because they have distinctive isotopes, an aspect critical to their successful identification in the APT measurements. The use of different metal combinations has the potential to cause variation in the type of metal sequence achieved within the MOF. The size difference of the mixed metals and its impact on bond lengths and angles exemplify chemical effects that introduce biasing into metal sequences. Another chemical effect explored in this study is the temperature of synthesis, by which the competition between mixing enthalpy (lattice matching) and configurational entropy (the number of ways metals may arrange themselves in a lattice) comes into play. The consequence of this biasing is that for a binary mixture of metals, one would expect sequences that deviate from randomness.

Accordingly, crystals of MOF-74 were synthesized in which the metal combination and synthesis temperature were varied: Co,Cd-MOF-74 (120°C), Co,Cd-MOF-74 (85°C), Co, Pb-MOF-74 (85°C), and Co,Mn-MOF-74 (85°C) (supplementary text S1.1). For each of these combinations and synthetic conditions, three crystals were measured in parallel by means of APT for a grand total of 12 crystals, where the molar fraction of Co (χ_{Co}) within each crystal ranged from 0.4 to 0.9 (table S1). The statistical average of metal molar fractions over all the crystals in a bulk sample was provided by inductively coupled plasma-atomic emission spectroscopy (ICP-AES) measurements and found to be 0.6 to 0.9 (table S2). The structure of the obtained MOF-74 crystals was confirmed with powder x-ray diffraction (fig. S1). The crystal size and morphology were measured and confirmed with scanning electron microscopy (SEM) (fig. S2). The two metal types in the mixed-metal MOF crystals were observed by means of energy-dispersive x-ray spectroscopy mapping and found to be distributed evenly on a mesoscopic level throughout the whole MOF crystals (fig. S3).

A higher resolution of the metal distributions in the crystals was achieved with APT, which combines field ion microscopy with

[1]Department of Chemistry, University of California, Berkeley, Berkeley, CA 94720, USA. [2]Materials Sciences Division, Lawrence Berkeley National Laboratory, Berkeley, CA 94720, USA. [3]Kavli Energy NanoSciences Institute at Berkeley, Berkeley, CA 94720, USA. [4]Berkeley Global Science Institute, Berkeley, CA 94720, USA. [5]Institute for Materials, Ruhr-Universität Bochum, Universitätsstraße 150, 44801 Bochum, Germany. [6]University of California, Berkeley–King Abdulaziz City for Science and Technology (KACST) Joint Center of Excellence for Nanomaterials for Clean Energy Applications, KACST, Riyadh 11442, Saudi Arabia.
*Corresponding author. Email: tong.li@ruhr-uni-bochum.de (T.L.); yaghi@berkeley.edu (O.M.Y.)

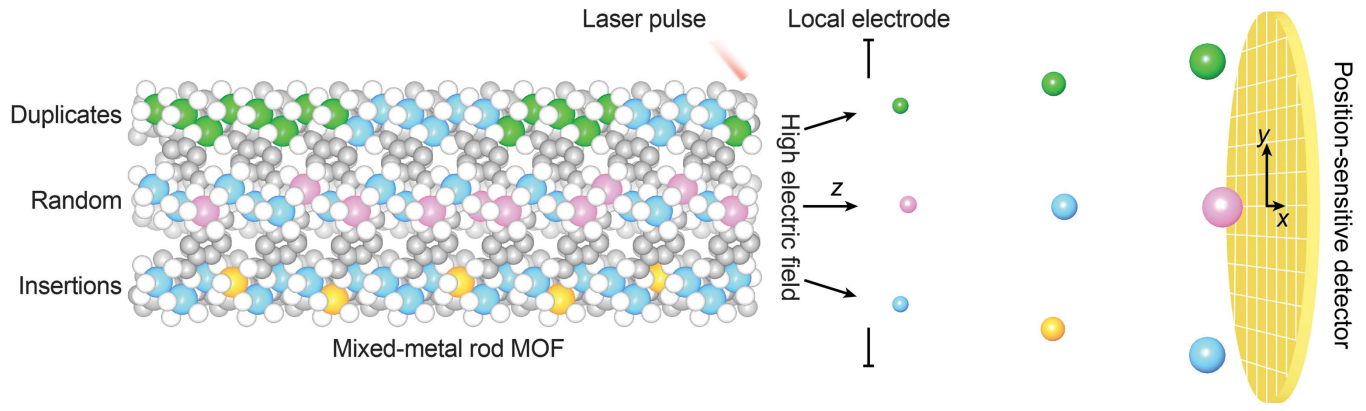

Fig. 1. Experimental approach. Shown is the use of APT technique to determine the type of metal sequences that exist in mixed-metal MOFs containing metal-oxide rods as building units linked by organics. Separating the sample and the position-sensitive detector is a local electrode for modulating the electric field. Metals of different kinds are shown in blue, green, pink, and orange, respectively. Carbon (C) and oxygen (O) atoms are colored in gray and white, respectively. The sizes of the atoms are arbitrarily adjusted for better illustration of metal sequence.

mass spectrometry (*30*) and has been used for mapping elemental distributions in alloys (*31*–*33*) and metal-oxide minerals (*22*–*25*). Triggered by laser pulsing, ions in the sample are sequentially evaporated from the surface by field effect and projected onto a position-sensitive detector, with their mass-to-charge ratio recorded with time-of-flight mass spectrometry (Fig. 1). Accordingly, both the chemical identity and geometrical position of these ions are determined and thereby used to construct a three-dimensional (3D) map for structural study of the sample.

In this work, we show that we can use APT to map the metal sequences within the 12 crystals in real space and that the analysis of these sequences gives four types of metal sequence, depending on the specific metal combination and the synthesis temperature: random (Co, Cd, 120°C), short duplicates of two to four metals (Co, Cd, 85°C), long duplicates of greater than four metals (Co, Pb, 85°C), and insertions of a single metal into duplicates of another metal (Co, Mn, 85°C). Our analysis distinguished different sequences by using reconstituted metal chains (with ~84% accuracy) based on the experimental 3D map obtained from APT. Because APT has not before been used in the analysis of MOFs, we outline the basic methodology and the challenges that we had to overcome to obtain meaningful information for metal sequences in mixed-metal MOFs by using APT.

An important goal for the APT analysis was to distinguish different types of metal sequence in the mixed-metal rod MOF. Pairwise multicomponent short-range order (PM-SRO) has been used to describe how the observed arrangements of metals in alloys differ from the uniformity implied by their nominal stoichiometry (*34*, *35*). It is this parameter that we aimed to determine so as to help in identifying sequence types. The PM-SRO parameter is defined as

$$\alpha_m^{AB} = \frac{p_m^{AB} - \chi_B}{\delta^{AB} - \chi_B}$$

where p_m^{AB} is the observed frequency of finding a B-type atom at the position m from an origin placed on an A-type atom, and χ_B represents the molar fraction of B in the mixture. δ^{AB} equals 1 if $A = B$ and 0 if $A \neq B$. In our study, the latter case was not considered because we always compared the same metal across the sequence for determining their duplicate size; thus, in our analysis $A = B$ always. A positive value of α^{AB} indicates the tendency toward segregation of A and B, whereas a negative one suggests intermingling (mixing) of these atoms. It would be zero if the distribution of A and B were randomly uniform.

In contrast to bulk metals and metal oxides, the analysis space in our rod MOFs is reduced to one dimension, and m can only take on integer values, representing the distance between metal pairs on a chain (supplementary text S2.1, fig. S4, and table S3). To use the PM-SRO parameter α, the span of m that keeps $\alpha > 0$ was examined and treated as the duplicate size predominating the metal sequence because it is expected to have a high probability for finding metals of the same type within a distance shorter than the duplicate size. We define sequence types as long duplicates, short duplicates, insertions, or random when they have excessive duplicates (compared with randomness) in size >4, between 2 and 4, 1, or 0, respectively. This definition has the advantage of having an unbiased PM-SRO parameter α when only a subset of metals from a sample are detected, as is typically the case for APT measurements. Even though in our experiments the detection efficiency is 52%, it will not bias the measurement of α, as evidenced by measuring the effect of random data removal on simulated sequences (supplementary text S2.2 and figs. S5 to S8). Through our APT experiments, the 52% detection efficiency still yielded more than 5000 metal ions identified from each MOF-74 crystal, a data size sufficient to provide an accuracy of α within ± 0.03 for a 95% confidence level, as calculated with the Johnson-Klotz Markov chain method (*36*) (supplementary text S2.3 and table S4). The unbiased and accurate measurement of α allows for robust identification of metal sequence types.

We also analyzed the distribution of duplicate sizes by directly counting duplicates in metal sequences, which provided further guidance on assigning sequence types (supplementary text S2.4). Unlike the PM-SRO parameter, duplicate size distribution is susceptible to data loss (figs. S5 to S8). Because of the 52% detection efficiency, the obtained duplicate size distribution underestimates the level of deviation from randomness; the real sequence type of metals in the crystals deviates more from randomness than what the distribution of duplicate size tells us. Therefore, the distribution of duplicate size should be used with caution and be combined with analysis of the PM-SRO parameter.

In mapping metals by using APT, one must be cognizant of spatial resolutions of ~0.2 nm for depth (z axis, the vertical direction) and 0.5 to 1 nm for lateral (xy plane) (Fig. 1). The lower resolution of the latter is caused by trajectory aberrations and local magnification effects (*37*), blurring out the in-plane position of atoms from their true lattice sites (*23*). Nevertheless, the depth resolution along z is sufficiently high to distinguish atoms emanating from different depths (*38*). In this study, we took advantage of the high depth resolution by aligning the rod

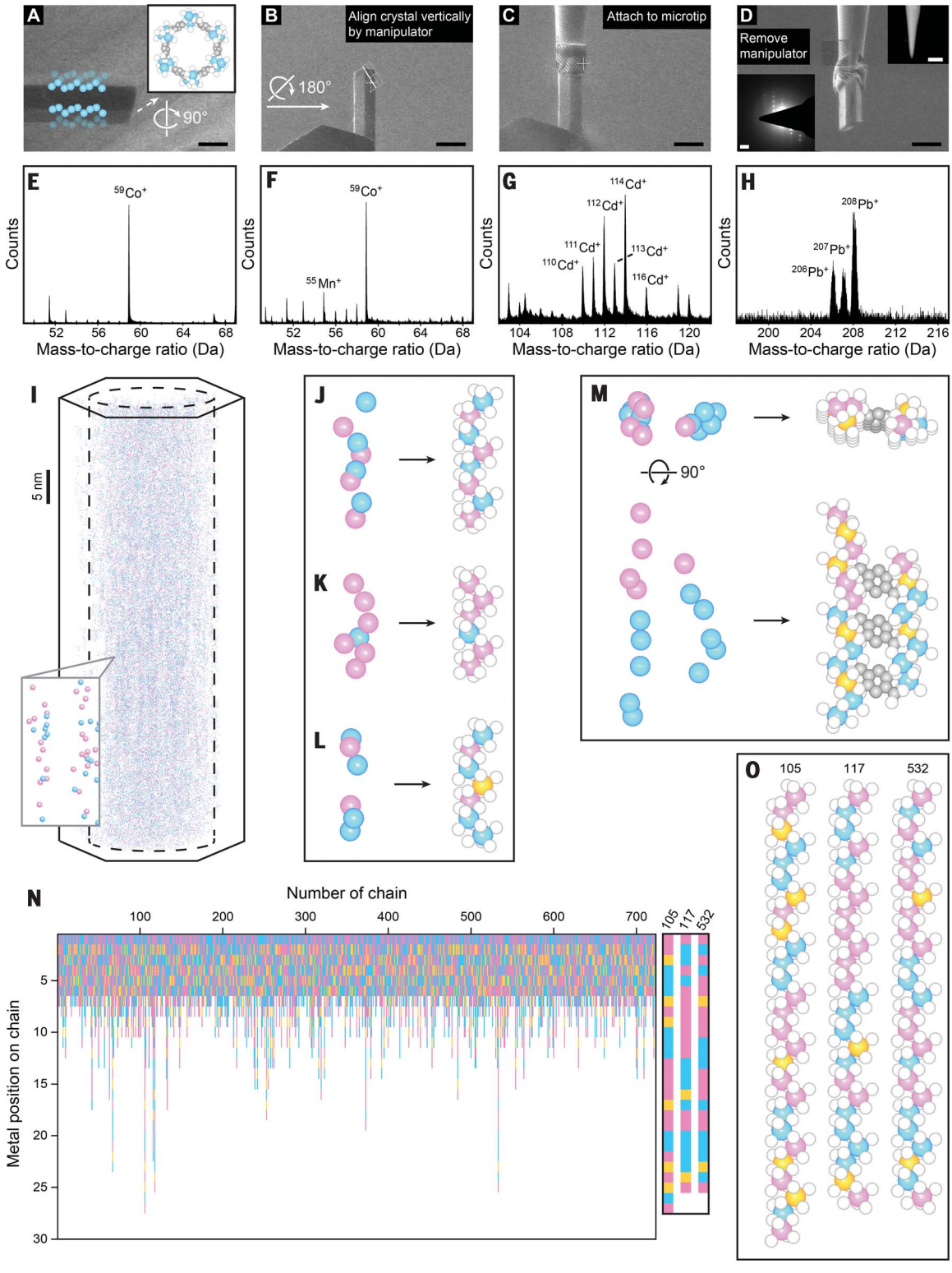

Fig. 2. APT measurement and sequencing of metals in a Co,Cd-MOF-74 single crystal. (**A** to **D**) The APT sample preparation procedure was recorded by a snapshot mode in a dual-beam focused ion beam/SEM. A single crystal of Co,Cd-MOF-74 was (A) attached to a nanomanipulator, (B) aligned vertically, (C) welded to a Si microtip, (D) detached from the nanomanipulator, and last [(D), top right inset], sharpened into a tip shape. Six of the metal-oxide rods in the MOF crystal, enclosing a hexagonal pore, are drawn [(A), inset] and arbitrarily enlarged to overlay on the crystal for better illustration of its long dimension, which is parallel to the rods. [(D), bottom-left inset] The selected-area electron diffraction pattern obtained from the APT tip is indexed in fig. S9 according to the crystal structure of MOF-74. Scale bars, 2 μm; (D), top right inset, 0.4 μm; and (D), bottom left inset, 2 nm^{-1}. (**E** to **H**) The mass spectra of MOF-74 samples identified (E) $^{59}Co^+$, (F) $^{55}Mn^+$, (G) Cd^+, and (H) Pb^+ isotopes, and other species (figs. S11 to S24). (**I**) 3D-APT reconstruction shows all the metals detected (56,605 in total) from a single crystal of Co,Cd-MOF-74 in a 3D space of 20 by 20 by 70 nm. A zoomed-in region where there are metal chains is shown. (**J** to **L**) Metal chains extracted from the raw data were reconstituted into metal-oxide rod SBUs, yielding (J) a good match, (K) a redundant metal, and (L) a missing metal. (**M**) The neighboring metal chains were reconstituted into rods that are connected by organic linkers. (**N**) The sequence of 723 metal chains is presented in a bitmap, where the color of squares represents the identity of metals located in the chain. Among these metal sequences, those of the 105th, 117th, and 532nd metal chains are displayed with magnification. (**O**) The metal-oxide rods reconstituted from the 105th, 117th, and 532nd metal chains. Color code: Co, blue; Cd, pink; missing metals, orange; O, white; and C, gray. The sizes of atoms follow the same condition as in Fig. 1.

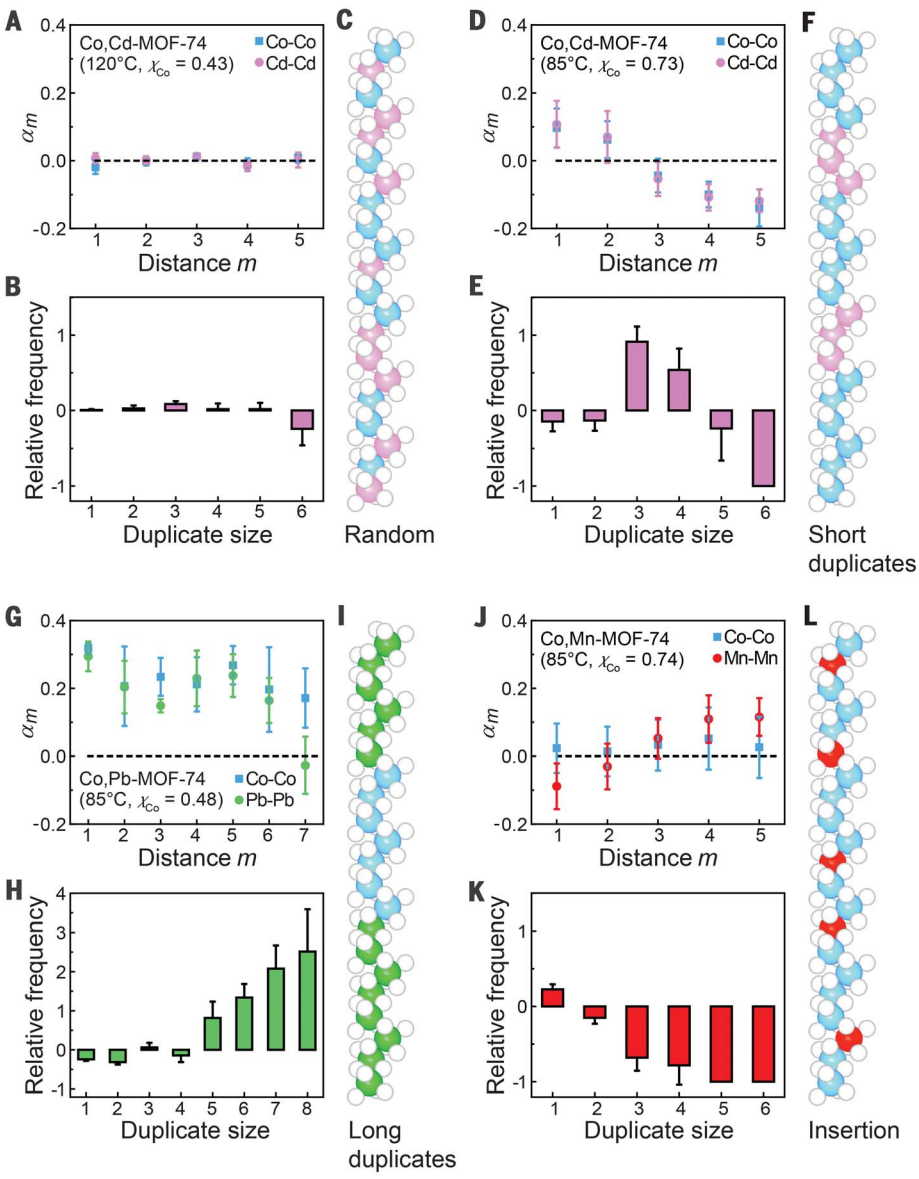

Fig. 3. Statistical analysis of metal arrangements in multivariate MOF-74. (**A**) The PM-SRO parameter α plotted against the distance *m* between metal pairs in Co,Cd-MOF-74 (120°C). (**B**) The histogram of duplicate sizes in this MOF crystal. Relative frequency is calculated by normalizing the difference between the number of duplicates observed and that simulated according to uniform distribution. (**C**) The structure model of metal-oxide rod SBUs in a random sequence for Co,Cd-MOF-74 (120°C). (**D** to **F**) The α plot, duplicate size histogram, and structural model for Co,Cd-MOF-74 (85°C). (**G** to **I**) The α plot, duplicate size histogram, and structural model for Co,Pb-MOF-74 (85°C). (**J** to **L**) The α plot, duplicate size histogram, and structural model for Co, Mn-MOF-74 (85°C). Error bars were calculated according to five independent runs of data processing, and the uncertainty was derived from the stochastic nature of the *k*-means clustering algorithm. Some error bars are not shown because these duplicate sizes are consistently not found (relative frequency remained −1 without variability). Color code: Co, blue; Cd, pink; Pb, green; Mn, red; and O, white.

SBUs of the MOF along the longest dimension of the hexagonal-prism crystal perpendicular to the detection plane (Fig. 2, A to D, and supplementary text S3.1). As such, the chain of metals in the metal-oxide rod SBUs are subject to metal sequence "reading" along the measurement *z* axis. The final MOF specimen was sharpened by using a dual-beam focused ion beam into a tip (diameter of <100 nm) (Fig. 2D, top right inset) suitable for APT measurements, without loss of crystallinity, as confirmed by means of electron diffraction (Fig. 2D, bottom left inset, and fig. S9).

We performed APT on all 12 crystals (supplementary text S3 and fig. S10). All the constituent metals were identified from mass spectra because their isotopes have mass-to-charge ratios distinctive from that of the complex fragments generated from the organic linker during the APT experiment (Fig. 2, E to H; figs. S11 to S24; and table S5). We choose here as an illustrative example Co,Cd-MOF-74 (120°C), where the position and the chemical identity of 56,605 metals were collected and mapped (Fig. 2I). A prerequisite for the reconstitution of rod SBUs is that the lateral-position inaccuracy of APT not be too large to turn data into complete randomness, and thus chains of metal can still be discernable from their 3D map. An aspect that works in our favor is the choice of a rod MOF as an object for this study. The separation of the metal rods through organics works against the unfavorable contributions of the lateral resolution because the overlap in detecting metals on different rods is reduced.

To assess whether the distribution of metals statistically displays a linear trend, we evaluated their clustering tendency along different directions. For a metal chain propagating along the *z* direction, its projection onto the *xy* plane displays a cluster where the metals appear on top of each other (eclipsed). By contrast, its projections onto the *xz* or the *yz* plane would assume a linear configuration, with higher position variance than that of a cluster. To distinguish this anisotropy for our sample, the 3D map containing the identity of the metals as well as their positions was flattened into each of the three Cartesian planes (supplementary text S4.1 and S4.2). These data were input into a *k*-means clustering algorithm for partitioning metals into clusters on the basis of their in-plane proximity. This gave the variance in metal positions within a cluster, which was found to be lower in the *xy* plane (as expected owing to the metals being eclipsed), compared with those in the *xz* and *yz* plane, all of which are lower than that of a randomly uniform distribution (fig. S25). The tendency

that metals are preferentially clustered along the z axis and therefore arranged in a linear pattern in this direction allowed the reconstitution of the rod SBUs in the crystal of Co, Cd-MOF-74 (120°C).

The reconstitution of metal chains was done by developing an algorithm specifically designed to assign the metals from the 3D map into chains (supplementary text S4.3, figs. S26 and S27, and table S6). The metals belonging to the same cluster partitioned by the k-means algorithm on the xy plane will constitute a chain if their vertical distances match the crystallographic vertical distance of 2.25 Å between two neighboring metals in the structure of MOF-74. On the basis of this distance criterion, metals falling within ±50% (considering the depth resolution of APT measurements) were assumed to be neighbors, assigned to the same metal chain, and reconstituted together into a metal-oxide rod (Fig. 2J). However, if within this range more than one metal was found, the one closest to the crystallographic position was chosen to minimize the chance of mistaking it with an off-position metal that actually belongs to a neighboring chain (Fig. 2K). If no metal satisfied this distance criterion, a missing ion was assumed to be in that position and arbitrarily placed to accommodate the 52% detection efficiency (Fig. 2L). This allowed for the continuous search for the next metal in the chain. The search for metals belonging to a chain terminated when two missing metals were found in a row. Then, the metal assignment for the next chain was initiated until the entire 3D map of metal was exhausted. If two separate metal chains were spaced by the size of a phenylene ring (5.6 Å), they were reconstituted into neighboring rod SBUs connected by organic linkers (Fig. 2M and supplementary text S4.4). All the metal chains thus extracted from the 3D map are shown in Fig. 2N. Among the 723 chains examined in this single crystal, the longest one (the 105th) was found to be 27 metals in length and has 9 Co, 12 Cd, and 6 missing metals (Fig. 2O). Even though the detection efficiency was 52%, the reason that the number of missing metals appears low has to do with our choice of long chains of relatively fewer missing metals to proceed to the next sequence analysis (supplementary text S4.5). This helped in increasing the accuracy of metal-chain reconstitution.

We used the developed chain-searching algorithm to confirm the proper alignment of MOF crystals during sample preparation. The alignment of MOFs during sample preparation (Fig. 2, A to D) might not be 100% accurate, causing the inaccuracy in chain searching. The orientation of chains along the z direction was corroborated by intentionally rotating the 3D map along the x or y axis to examine whether this operation yields fewer number of chains (supplementary text S4.7). When this was done for the crystal of Co,Cd-MOF-74 (120°C), we found that it was aligned as we expected (fig. S28 and table S7). These results indicate that the metal-oxide rods were aligned along the z axis (misalignment angle < 5°) and were structurally preserved despite some lateral deviation during the measurements.

To evaluate the impact of trajectory aberration on the accuracy of assigning metals in chains, we applied the same algorithm presented above to a virtual 3D map of metals that was simulated by adding a Gaussian noise (*23*) to their lateral crystallographic positions (supplementary text S4.8). The positional deviation resulting from the added noise was chosen to match the simulated data with the experimental ones in terms of the within-cluster metal-position variance obtained from the k-means algorithm (figs. S29 and S30). By tracking the number of metals that were correctly assigned into chains, the accuracy was estimated to be ~81% (table S8). When only metal chains with few missing atoms and a small variation in lateral position (constituent metals are more eclipsed) were used for metal rod reconstitution, the accuracy can be further enhanced to ~84%. Whereas a lower accuracy will turn regularity into randomness, this accuracy was found sufficient to allow us to observe recognizable deviation from randomness in metal sequences.

To determine the sequence type of our samples, the PM-SRO parameter α was calculated for the obtained reconstituted chains. Its value was found to remain near zero at different distances for Co,Cd-MOF-74 (120°C) (Fig. 3A), corresponding to the existence of a random sequence of metals (Fig. 3C). Consistently, the histogram of duplicate sizes within this sequence obtained through direct counting was in good agreement with those of the sequences simulated through uniform distribution (Fig. 3B).

A crystal of the same metal combination but synthesized at a lower temperature (85°C) showed duplicates for both Co and Cd (Fig. 3F), evidenced by the enhanced frequency of finding metals of the same type within a distance of 2 and in a lower frequency beyond this distance (Fig. 3D). This result indicates the dominance of duplicates in the size of 3, which was corroborated by the duplicate size histogram (Fig. 3E). These types of sequence were found to be consistent among crystals made under the same synthetic conditions (fig. S31), although their molar fraction of metals varies.

The physical nature behind the observed metal arrangements in multivariate MOF-74

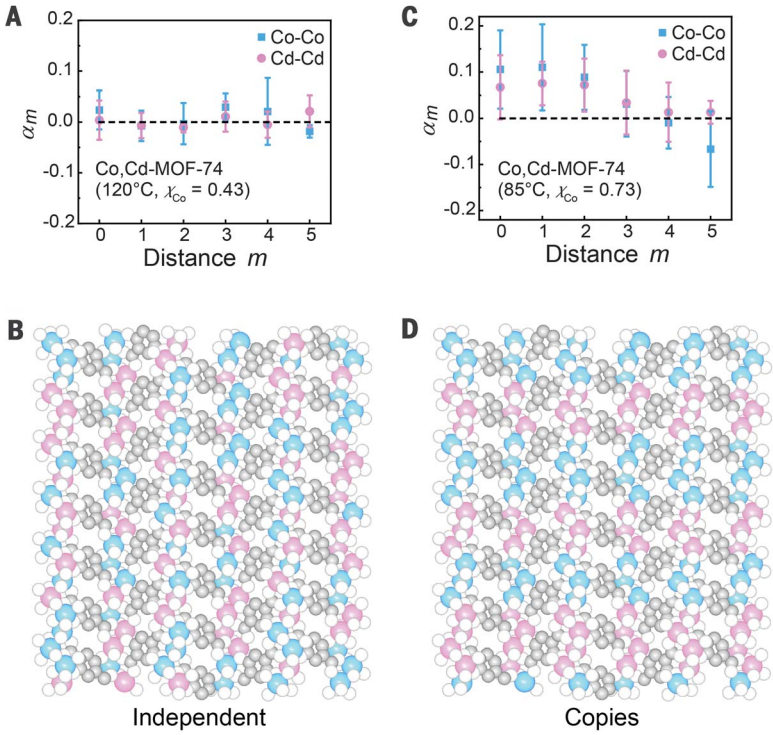

Fig. 4. The metal arrangement across neighboring metal-oxide rods. (**A**) The PM-SRO parameter α for describing the distribution of metal pairs on the neighboring rods in Co,Cd-MOF-74 (120°C). (**B**) The structure model of Co,Cd-MOF-74 (120°C), illustrating the independent type of metal arrangement across rods. (**C**) The PM-SRO parameter for Co,Cd-MOF-74 (85°C). (**D**) The structure model of Co,Cd-MOF-74 (85°C), displaying sequence copies across rods. Color code: Co, blue; Cd, pink; O, white; and C, gray.

is rationalized by an energy diagram (supplementary text S5.2 and fig. S32). Fundamentally, the distinct metal sequences represent intermediate states in the continuum between complete phase separation and ordered alternation in a single phase. A random sequence maximizes the configurational entropy (*39*), which could be translated into the minimum free energy under the assumption that the enthalpy change involved in the permutation of components is negligible. This assumption does not hold true, for example, when metals of varying sizes are mixed into an alloy. The Hume-Rothery Rule requires that the atomic radius of the metals in solid-solution alloys must differ by no more than 15% (*40*). The requirement of similar ion radii has also been observed for metal oxides, with the difference being up to 25% (*41*–*43*). Otherwise, the generated lattice mismatch causes substantial strain, and the resultant energy cost drives the system to deviate from the entropic maximum. Within metal-oxide rods in MOF-74, the partial replacement of Co (0.65 Å in radius for +2 ions) by the larger Cd (0.95 Å) induces distorted metal-O bonds (*44*), and consequently, a duplicate sequence is favored to minimize the energy penalty. When we performed synthesis at a higher temperature, the contribution of configuration entropy became more dominant, thus making the entropy well steeper (fig. S32). Therefore, the combination of Co and Cd—which grows into short duplicates at low synthesis temperature—at a higher temperature falls into the regime of random sequences.

Although duplicate sizes as large as 5 and 6 were mostly absent from Co,Cd-MOF-74 (85°C), these long duplicates and even longer ones were indeed highly populated in Co,Pb-MOF-74 (85°C), where instead shorter duplicates were unfavorable (Fig. 3, H and I). This is evidenced by the values of the PM-SRO parameter, where we found that they remained positive in distant regions (Fig. 3G). When the larger Pb (1.19 Å) was used instead of Cd in their combination with Co, metal mixing involved more substantial size mismatch and therefore yielded longer duplicate sizes, as expected. The size difference of 83% between Co and Pb in MOF-74 far exceeds the 25% limit observed for solid-solution metal oxides, without entering the phase separation stage. This crystal having equal amounts of metals and the observation of long duplicates rather than random are evidence of the importance of chemical effects in biasing sequences and the power of APT in illuminating how metals are mixed in multimetallic MOFs.

Last, insertion sequences (Fig. 3L) were found for Co,Mn-MOF-74 (85°C), where one metal prefers to insert into duplicates of the other, thus leading to a decrease in the segregation of the inserting metal (Fig. 3K) and a corresponding increase in PM-SRO parameters for longer distances (Fig. 3J). The insertion sequence indicates a possible attractive interaction between Co and Mn, which have similar sizes (0.65 and 0.67 Å, respectively). For Co,Pb-MOF-74 and Co,Mn-MOF-74, we halved the analyzed crystals and found that there was no disparity in sequence type between their respective segments (fig. S33).

We further extended our method to the analysis of sequences of neighboring chains (Fig. 4). Other than the metal sequences within the metal-oxide rods, there are in general three different ways to spatially arrange these sequences: copies (the same metal sequences in neighboring rods that are aligned with respect to each other), inverse (the metal type in one sequence is displaced by another metal type in neighboring rods), and independent (no correlation between the sequences on neighboring rods) (fig. S34). To decipher the metal arrangements across neighboring rods, we performed the same PM-SRO analysis on the obtained sequences except for the origin used for defining position, which we placed on the rod neighboring the one under evaluation (supplementary text S2.1). A distance of zero means that the two metals are aligned at the same height on neighboring rods. According to the interchain PM-SRO parameters, Co,Cd-MOF-74 (120°C) displayed an independent metal arrangement between rods (Fig. 4, A and B). However, in Co,Cd-MOF-74 (85°C), short duplicates of the same type were found to be aligned between neighboring rods, constituting a copy arrangement (Fig. 4, C and D).

REFERENCES AND NOTES

1. H. Deng *et al.*, *Science* **327**, 846–850 (2010).
2. L. J. Wang *et al.*, *Inorg. Chem.* **53**, 5881–5883 (2014).
3. O. M. Yaghi, M. J. Kalmutzki, C. S. Diercks, *Introduction to Reticular Chemistry: Metal-Organic Frameworks and Covalent Organic Frameworks* (Wiley-VCH, 2019).
4. Z. Dong, Y. Sun, J. Chu, X. Zhang, H. Deng, *J. Am. Chem. Soc.* **139**, 14209–14216 (2017).
5. Y. B. Zhang *et al.*, *J. Am. Chem. Soc.* **137**, 2641–2650 (2015).
6. T. Li *et al.*, *Microporous Mesoporous Mater.* **272**, 101–108 (2018).
7. Q. Liu, H. Cong, H. Deng, *J. Am. Chem. Soc.* **138**, 13822–13825 (2016).
8. A. M. Fracaroli *et al.*, *J. Am. Chem. Soc.* **138**, 8352–8355 (2016).
9. Q. Xia *et al.*, *J. Am. Chem. Soc.* **139**, 8259–8266 (2017).
10. L. M. Aguirre-Díaz *et al.*, *J. Am. Chem. Soc.* **137**, 6132–6135 (2015).
11. L. Wang *et al.*, *ACS Appl. Mater. Interfaces* **8**, 16736–16743 (2016).
12. S. Lin *et al.*, *Science* **349**, 1208–1213 (2015).
13. T. M. Osborn Popp, O. M. Yaghi, *Acc. Chem. Res.* **50**, 532–534 (2017).
14. H. Furukawa, U. Müller, O. M. Yaghi, *Angew. Chem. Int. Ed.* **54**, 3417–3430 (2015).
15. N. L. Rosi *et al.*, *J. Am. Chem. Soc.* **127**, 1504–1518 (2005).
16. A. Schoedel, M. Li, D. Li, M. O'Keeffe, O. M. Yaghi, *Chem. Rev.* **116**, 12466–12535 (2016).
17. S. R. Caskey, A. G. Wong-Foy, A. J. Matzger, *J. Am. Chem. Soc.* **130**, 10870–10871 (2008).
18. P. D. C. Dietzel *et al.*, *Chem. Commun.* **41**, 5125–5127 (2008).
19. D. Britt, H. Furukawa, B. Wang, T. G. Glover, O. M. Yaghi, *Proc. Natl. Acad. Sci. U.S.A.* **106**, 20637–20640 (2009).
20. F. Fathieh *et al.*, *Sci. Adv.* **4**, eaat3198 (2018).
21. N. Hanikel *et al.*, *ACS Cent. Sci.* **5**, 1699–1706 (2019).
22. B. Scherrer *et al.*, *Chem. Mater.* **32**, 1031–1040 (2020).
23. J. E. Schmidt, L. Peng, J. D. Poplawsky, B. M. Weckhuysen, *Angew. Chem. Int. Ed.* **57**, 10422–10435 (2018).
24. D. E. Perea *et al.*, *Nat. Commun.* **6**, 7589 (2015).
25. A. Devaraj *et al.*, *Nat. Commun.* **6**, 8014 (2015).
26. X. Kong *et al.*, *Science* **341**, 882–885 (2013).
27. C. Castillo-Blas *et al.*, *Sci. Adv.* **3**, e1700773 (2017).
28. Y. Zhu *et al.*, *Nat. Mater.* **16**, 532–536 (2017).
29. W. Schrimpf *et al.*, *Nat. Commun.* **9**, 1647 (2018).
30. B. Gault, M. P. Moody, J. M. Cairney, S. P. Ringer, *Atom Probe Microscopy*, vol. 160, Springer Series in Material Science (Springer, 2012).
31. Y.-S. Chen *et al.*, *Science* **355**, 1196–1199 (2017).
32. M. Kuzmina, M. Herbig, D. Ponge, S. Sandlöbes, D. Raabe, *Science* **349**, 1080–1083 (2015).
33. Y.-S. Chen *et al.*, *Science* **367**, 171–175 (2020).
34. D. de Fontaine, *J. Appl. Cryst.* **4**, 15–19 (1971).
35. A. V. Ceguerra *et al.*, *Acta Crystallogr. A* **68**, 547–560 (2012).
36. C. A. Johnson, J. H. Klotz, *Technometrics* **16**, 483–493 (1974).
37. F. Vurpillot, A. Bostel, D. Blavette, *Appl. Phys. Lett.* **76**, 3127–3129 (2000).
38. B. Gault, M. P. Moody, J. M. Cairney, S. P. Ringer, *Mater. Today* **15**, 378–386 (2012).
39. D. A. Porter, K. E. Easterling, M. Y. A. Sherif, *Phase Transformation in Metals and Alloys* (CRC Press, ed. 3, 2009).
40. W. B. Pearson, *A Handbook of Lattice Spacings and Structures of Metals and Alloys*, *International Series of Monographs on Metal Physics and Physical Metallurgy*, vol. 4 (Pergamon, 1958).
41. A. Urban, A. Abdellahi, S. Dacek, N. Artrith, G. Ceder, *Phys. Rev. Lett.* **119**, 176402 (2017).
42. X.-W. Zhang, Q. Wang, B.-L. Gu, *J. Am. Ceram. Soc.* **74**, 2846–2850 (1991).
43. L. Zhang *et al.*, *J. Power Sources* **185**, 534–541 (2008).
44. J. D. Howe *et al.*, *J. Phys. Chem. C* **121**, 627–635 (2017).

ACKNOWLEDGMENTS

We thank A. Kostka [Zentrumfür Grenzflächendominierte Höchstleistungswerkstoffe (ZGH)] for the TEM experiment; Y. Wei (Stanford University) for the assistance of data processing; and B. Rungtaweevoranit, H. Lyu, and C. S. Diercks (members of the Yaghi Laboratory) for SEM measurements and helpful discussions. T.L. acknowledges ZGH at Ruhr University Bochum for the access to infrastructure (FEI Helios G4 CX FIB/SEM and Cameca LEAP 5000 XR). We thank G. Prieto (ITQ Institute of Chemical Technology), F. Schüth (Max-Planck-Institut für Kohlenforschung), B. Gault [Max-Planck-Institut für Eisenforschung GmbH (MPIE)], and D. Raabe (MPIE) for initiating the collaboration and providing infrastructures for preliminary trials. **Funding:** This research was supported by King Abdulaziz City for Science and Technology (Center of Excellence for Nanomaterials and Clean Energy Applications). **Author contributions:** O.M.Y., Z.J., and T.L. designed the project. Z.J. synthesized MOF crystals. T.L. performed APT measurements. Z.J. and T.L. analyzed the APT data. Z.J., T.L., and O.M.Y. prepared the manuscript. **Competing interests:** None declared. **Data and materials availability:** All data needed to evaluate the conclusion in the paper are present in the paper or the supplementary materials. Code written for the chain searching algorithm is available at https://github.com/sequencingMOF/metalchain.

SUPPLEMENTARY MATERIALS

science.sciencemag.org/content/369/6504/674/suppl/DC1
Materials and Methods
Supplementary Text
Figs. S1 to S34
Tables S1 to S8
References (*45*, *46*)

9 September 2019; resubmitted 9 March 2020
Accepted 17 June 2020
10.1126/science.aaz4304